The 2021 Pacific Northwest heat wave and associated blocking: meteorology and the role of an upstream cyclone as a diabatic source of wave activity

Emily Neal[1], Clare S. Y. Huang[1], and Noboru Nakamura[1]

[1]University of Chicago

November 22, 2022

Abstract

We investigate the meteorological and dynamical conditions that led to the extreme heat in the Pacific Northwest from late June to early July 2021. The extreme heat was preceded by an upper-level atmospheric blocking that snatched a warm pool of air from lower latitudes. A heat-trapping stable stratification ensued within the block, raising the surface temperatures significantly. An upper-tropospheric wave breaking and the concomitant surface cyclogenesis off the coast of Alaska initiated the block formation. The regional local wave activity budget reveals that a localized diabatic source associated with this storm critically contributed to the block by enhancing the zonal wave activity flux downstream, whose convergence over Canada drove the blocking. A simple model-based reconstruction predicts a 41 percent reduction in strength and a 10-degree eastward displacement of the block when the upstream diabatic source is reduced by just 30 percent.

The 2021 Pacific Northwest heat wave and associated blocking: meteorology and the role of an upstream cyclone as a diabatic source of wave activity

Emily Neal [1], Clare S. Y. Huang [1] and Noboru Nakamura [1]

[1]Department of the Geophysical Sciences, University of Chicago

Key Points:

- A strong atmospheric blocking preceded the Pacific Northwest heat wave in late June 2021, setting up a heat-trapping stable stratification
- An upstream cyclogenesis provided a critical diabatic source of wave activity flux, which converged downstream to create the block
- When the upstream diabatic forcing is artificially reduced, the reconstructed blocking weakens dramatically and shifts downstream

Corresponding author: Noboru Nakamura, nnn@uchicago.edu

Abstract

We investigate the meteorological and dynamical conditions that led to the extreme heat in the Pacific Northwest from late June to early July 2021. The extreme heat was preceded by an upper-level atmospheric blocking that snatched a warm pool of air from lower latitudes. A heat-trapping stable stratification ensued within the block, raising the surface temperatures significantly. An upper-tropospheric wave breaking and the concomitant surface cyclogenesis off the coast of Alaska initiated the block formation. The regional local wave activity budget reveals that a localized diabatic source associated with this storm critically contributed to the block by enhancing the zonal wave activity flux downstream, whose convergence over Canada drove the blocking. A simple model-based reconstruction predicts a 41 percent reduction in strength and a 10-degree eastward displacement of the block when the upstream diabatic source is reduced by just 30 percent.

Plain Language Summary

From late June to early July 2021, an unprecedented heat wave enveloped the Pacific Northwest, causing over 1000 deaths. We investigate the meteorological condition and physical processes responsible for this event. Persistent meandering of the upper-level jet stream (blocking anticyclone) established a warm, stagnant column of air ('heat dome') over the Pacific Northwest, trapping heat near the surface. Somewhat counter-intuitively, the blocking anticyclone itself grew out of a cyclone that developed upstream (Gulf of Alaska) a few days prior, and the heat released during the formation of clouds in this storm played an essential role in fueling the blocking anticyclone (and heat wave) downstream. To the extent that blocking anticyclones in summer are fueled by condensation of moisture, we can expect them and associated heat waves to intensify as climate warms and the atmosphere contains more water vapor.

1 Introduction

The heat wave that enveloped the Pacific Northwest from late June through early July 2021 delivered unprecedented temperatures to the normally cool region — 108°F (42°C) in Seattle, 116°F (47°C) in Portland — and claimed over 1000 lives mostly in British Columbia (AON, 2021). One preliminary study puts it in a 1-in-1000 years event category (Philip et al., 2021). In the present study, we first provide an overview of the atmospheric conditions that led to the extreme heat event. As with most heat waves in the midlatitudes (Fang & Lu, 2020), this event was associated with an anomalous behavior of the jet stream (atmospheric blocking). We will show that the formation of an upper-level blocking preceded the extreme surface temperatures by 2-3 days, demonstrating a top-down thermodynamic control of blocking on the surface temperatures. We will then analyze the regional budget of local wave activity (LWA) (Huang & Nakamura, 2016, 2017, hereafter HN16 and HN17) to elucidate the dynamics behind the block formation. In particular, we will highlight the diabatic source of wave activity associated with an upstream cyclogenesis that contributed significantly to this unusually strong block. Our work complements previous trajectory-based studies (Pfahl et al., 2015; Steinfeld & Pfahl, 2019) to gain insight on the role of diabatic heating in blocking episodes. While the event lasted into July, we focus on the period leading up to the peak surface temperatures at the end of June. The demise and persistence of the event will be a topic of future study. The next section briefly describes the data and the wave activity diagnostic formalism. Section 3 summarizes the meteorological evolution during the event, followed by the wave activity diagnostic in Section 4. We conclude with a summary in Section 5.

2 Data and the wave activity diagnostic formalism

All data used in this study are derived from 6-hourly ERA5 reanalysis provided on 37 pressure levels with 1°× 1° horizontal resolution (Hersbach et al., 2020). The diagnostic framework follows the prescription of HN16 and HN17 (see also N. Nakamura & Huang, 2018; Valva & Nakamura, 2021, and Supporting Information of the present article). To quantify the jet stream's meander and identify blocks we use LWA, which measures the meridional displacement of quasigeostrophic potential vorticity (QGPV), q, from a zonally symmetric reference state

$$A(\lambda, \phi, z, t) = -\frac{a}{\cos\phi}\int_0^{\Delta\phi} q_e(\lambda, \phi+\phi', z, t)\cos(\phi+\phi')d\phi', \tag{1}$$

where (λ, ϕ, z, t) specifies longitude, latitude, pressure pseudoheight and time, a is planetary radius and q_e is the QGPV field relative to its reference state value at ϕ

$$q_e(\lambda, \phi+\phi', z, t) = q(\lambda, \phi+\phi', z, t) - q_{\mathrm{REF}}(\phi, z, t). \tag{2}$$

The reference state q_{REF} is obtained by zonalizing the wavy QGPV field through an area preserving map (N. Nakamura & Solomon, 2010). In Eq. (1), $\phi + \Delta\phi(\lambda, \phi, z, t)$ specifies the meridional location of the wavy QGPV contour whose value equals $q_{\mathrm{REF}}(\phi, z, t)$, and ϕ' is the displacement coordinate specific to, but independent of, ϕ.

The main draw for using LWA to quantify the waviness of the jet stream is that it possesses a relatively simple budget evaluable from data. In particular, the column budget of LWA is governed by (HN16, HN17)

$$\frac{\partial}{\partial t}\langle A\rangle\cos\phi = \underbrace{-\frac{1}{a\cos\phi}\frac{\partial\langle F_\lambda\rangle}{\partial\lambda}}_{\text{(I)}}\underbrace{-\frac{1}{a\cos\phi}\frac{\partial}{\partial\phi'}\langle F_{\phi'}\cos(\phi+\phi')\rangle}_{\text{(II)}}\underbrace{+\frac{f\cos\phi}{H}\left(\frac{v_e\theta_e}{\partial\tilde{\theta}/\partial z}\right)_{z=0}}_{\text{(III)}}\underbrace{+\langle\dot{A}\rangle\cos\phi}_{\text{(IV)}}, \tag{3}$$

where H is a constant scale height, f is the Coriolis parameter, and $\langle\cdots\rangle$ denotes density-weighted vertical average. Terms (I) and (II) on the RHS represent the zonal and meridional convergence of the column averaged wave activity flux. (See Supporting Information for the expressions for $\langle F_\lambda\rangle$ and $\langle F_{\phi'}\rangle$.) Term (III) is the vertical wave activity flux at the base of the atmosphere, where the meridional velocity and potential temperature are partitioned as $v_e = v$ and

$$\theta_e(\lambda, \phi+\phi', z, t) = \theta(\lambda, \phi+\phi', z, t) - \theta_{\mathrm{REF}}(\phi, z, t). \tag{4}$$

Here θ_{REF} is inverted hemispherically from q_{REF} (Supporting Information). Term (IV) is the nonadiabatic and non-quasigeostrophic sources-sinks. In practice, Term (IV) is evaluated as the residual of the budget. It is positive where there is net creation of QGPV anomalies (e.g. by convective transport of mass across isentropic surface, Madonna et al., 2014; Bueler & Pfahl, 2017) and negative where they are damped by mixing and friction (N. Nakamura & Zhu, 2010).

3 Meteorology

Figure 1 summarizes atmospheric conditions over the North Pacific/North American sector for 22-30 June 2021. Each row is a synopsis at 00 UTC (4 pm in the Pacific Northwest). On 22 June, the 250 hPa geopotential height and wind speed show an enhanced jet stream in the western Pacific around 40°N (column a). The jet is much weaker in the eastern Pacific, creating strong diffluence. The zonal variation of the jet speed is due partly to the zonally varying summertime sea surface temperatures (SSTs), which enforce relatively weak meridional temperature gradients in the eastern Pacific, both in the upper troposphere (450 hPa, columns b) and near surface (column c), leading to a generally weaker jet stream aloft. A diffluent jet sets up a favorable condition for block formation in the eastern Pacific (e.g. N. Nakamura & Huang, 2018).

On 24 June the jet stream buckles, initiating anticyclonic wave breaking. A tongue of warm air intrudes northward at 450 hPa, forming a 'warm conveyor belt' (Madonna et al., 2014). As we will see later (Figs. 3e and 3f), this coincides with surface cyclogenesis off the coast of Alaska. By 26 June the jet stream develops a large meander and forms a quasi-stationary anticyclone over the Pacific Northwest with a signature of an omega block (Woollings et al., 2018, Fig. 1). The tongue of warm air at 450 hPa rolls up to become a part of the blocking anticyclone. Similar evolution is also observed during winter blocks over Europe (e.g. H. Nakamura, 1994, Fig. 1). The upper tropospheric ridge and the associated warm core remain stationary until 30 June and gradually move downstream afterward (not shown). The block matures between 26-27 June, when the peak 250 hPa geopotential height reaches well over 11000 m, which we found in the top 0.01 percentile of all June-August values at 49°N based on 1979-2021 ERA5 reanalysis.

Until 26 June, 2-m temperature (column c) shows hotspots mostly in the southern part of western North America, where the land surfaces are dry. The peak temperatures gradually shift northward thereafter, and by 30 June they align with the location of the block. The highest surface temperatures in the region were reported between 28 June and 1 July (AON, 2021). Therefore, there appears a 2-3 day lag between the maturation of the block and the occurrence of the peak surface temperatures. Column d of Fig. 1 shows vertical cross sections of potential temperature at 49°N during the same period. They capture the emergence of an upper-level warm core associated with the block around 120°W 24-26 June. Subsequently the isentropes in the region move down, as highlighted by the 320 K contour, creating a vertically coherent 'heat dome.'

Figure 2 samples vertical potential temperature profiles at 119°W 49°N (east of Vancouver, BC), approximately at the center of the block, for 24-30 June. All profiles are sampled at 4 pm local time. On 24 June (before blocking), potential temperature is well mixed in the convective boundary layer up to $z = 4$ km (dotted curve). The arrival of the block on 26 June significantly raises potential temperature above 3 km (dashed curve). The overlying warm air caps the convective boundary layer at a lower altitude, effectively decreasing its heat capacity. As a result, daytime heating from the ground raises the temperature of the boundary layer by 12 K in 4 days until it deepens again, while the profile in the free troposphere remains nearly steady (dot-dashed and solid curves). This analysis strongly suggests that the extreme heat at surface was a thermodynamic response of the lower troposphere to an anomalously stable stratification aloft set up by the block and heating from below. In comparison, horizontal advection of temperature is deemed weak in the center of the block.

Column b of Fig. 1 suggests that the warm air above the boundary layer of the block originates from lower latitudes in the upstream. However, it is unclear how much of that warmth is attributable to latent heating. Previous studies based on trajectory analyses suggest that air parcels experience substantial latent heating in the warm conveyer belt of an extratropical cyclone (Madonna et al., 2014; Methven, 2015) and some of them end up in a blocking anticyclone downstream (Pfahl et al., 2015; Steinfeld & Pfahl, 2019). These studies also show that latent heating produces a significant amount of negative QGPV anomaly in the upper troposphere, an essential ingredient for blocking anticyclones. In the next section we examine the regional LWA budget and identify key processes that formed the block, including an upstream diabatic source of wave activity.

4 Regional wave activity budget

Here we apply the LWA diagnostic outlined in Section 2 for the formative stage of the block. To visualize the increase in LWA associated with the block, we integrate Eq.

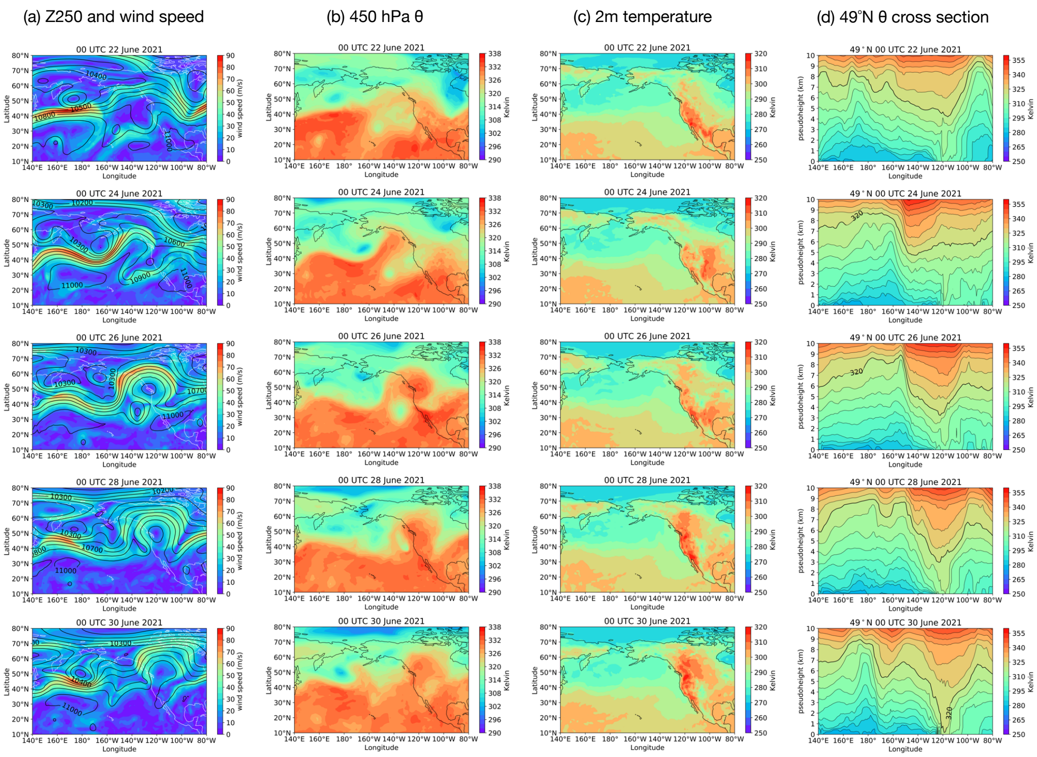

Figure 1. Circulation and temperature over North Pacific and North America 22-30 June 2021. Rows are, from top to bottom, 22, 24, 26, 28, 30 June at 00 UTC. Column a: 250 hPa geopotential height (contours in meters) and wind speed. Column b: 450 hPa potential temperature. Column c: 2-m temperature. Column d: vertical cross sections of potential temperature at 49°N (contour interval = 5 K). The vertical axis is pressure pseudoheight with $H = 8$ km (450 hPa = 6.4 km). Data source: ERA5 (Figs. 1-4).

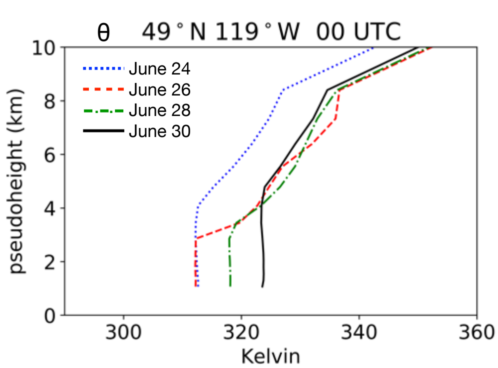

Figure 2. Vertical profiles of potential temperature at 119°W 49°N. The vertical axis is pressure pseudoheight with $H = 8$ km. Only values above the ground are shown. Dotted-blue: June 24. Dashed-red: June 26, Dot-dashed-green: June 28. Solid-black: June 30. All profiles are sampled at 00 UTC (4 pm local).

(3) from 20 to 26 June 00 UTC and diagnose the budget term-by-term. Figure 3a shows a map of the LHS, i.e., the change in column LWA from 20 to 26 June. The largest increase centers around the Pacific Northwest, roughly the location of the blocking anticyclone (Fig, 1 column a). The other maps show the time integrals of Term (III) (Fig. 3b), Terms (I)+(II) (Fig. 3c) and Term (IV) (Fig. 3d). The sum of Figs. 3b, 3c and 3d equals Fig. 3a (note a different color scale for Fig. 3a). Figure 3c and 3d also overlay the change in the 6-day average horizontal wave activity flux vector, $(\langle F_\lambda \rangle, \langle F_{\phi'} \rangle)$, from the previous 6-day period (14-20 June).

Except over the eastern Pacific, Term (III) is small (Fig. 3b). The dipole pattern in the eastern Pacific reflects the fact that in this region the perturbation potential temperature θ_e [Eq. (4)] is everywhere negative near the surface because of low SSTs. Therefore the Term (III) in Eq. (3) will be negative where the wind is southerly ($v_e > 0$) and positive where it is northerly ($v_e < 0$). The dipole pattern arises from a persistent anticyclonic circulation in this region during the period.

The block-related change in LWA is largely due to Terms (I) and (IV). Contributions from Term (II) prove also weak in the regions of interest, so the signal in Fig. 3c largely comes from Term (I). Figure 3c shows predominantly positive values (i.e. wave activity flux is convergent) over the western Canada. There are large negative values (divergence) off the coast of Alaska, and also broadly off the west coast of North America. The convergence of wave activity flux over Canada is compensated to a large degree by negative values of Term (IV) (Fig. 3d), presumably from dissipation of wave activity due to mixing and friction. Then there are very large positive values of Term (IV) off the coast of Alaska, which more than compensate the negative values of Terms (I), (II), (III) combined in the same region. This is believed to be the effect of latent heating associated with a cyclone that formed in this region 23-24 June. Figures 3e and 3f show, respectively, the outgoing longwave radiation (OLR) at the top of the atmosphere and column water (excluding vapor) overlaid with sea level pressure for 23 June. Both the minimum OLR and the maximum column water depict tall, comma-shaped clouds associated with a cyclone, in good agreement with the location of the local maximum in Term (IV) (Fig. 3d) and the warm conveyor belt (Fig. 1 column b, second panel).

Figures 3c and 3d also show enhanced eastward wave activity fluxes over the Pacific during this period. The enhancement is particularly pronounced in 45-60°N, and east of the Gulf of Alaska. All this suggests that latent heating off the coast of Alaska was a significant source of wave activity flux downstream, which then converged over the western Canada to form a block. Although the location of the block is somewhat south of the peak of flux convergence, the observed LWA budget at the center of the block still fits the above description: at 118°W 49°N, the 6-day change in column LWA is 54.1 ms^{-1}, and contributions from Terms (I)-(IV) are 102.2, -10.2, 1.0, -38.9 ms^{-1}, respectively. Therefore about 40 percent of flux convergence is compensated by frictional loss to produce the observed LWA change.

The process of block maturation is further elucidated in the Hovmöller diagrams of column LWA (Fig. 4a), zonal LWA flux (Fig. 4b), flux convergence [Terms (I)+(II), Fig. 4c] and residual [Term (IV), Fig. 4d] at 49°N. Column LWA has a quasistationary maximum around 235°E (125°W). This reflects waviness in low-altitude QGPV arising from large land-sea thermal contrast across the coastline. However, LWA increases significantly toward the end of June as the block forms (Fig. 4a). Prior to this, there is a broad enhancement of eastward wave activity flux in the upstream (Fig. 4b). The enhancement entails two distinct stages, labeled A and B. Stage A is characterized by a strong, but migratory maximum in flux with a corresponding flux convergence (Fig. 4c). Since the convergence is short-lived at a given location, it does not increase LWA significantly (Fig. 4a). Here the increased flux simply reflects an enhanced jet speed (top left panel of Fig. 1). Stage B, on the other hand, is initiated by a local diabatic source that spans 22-24 June between 200-220°E (140-160°W, Fig. 4d). This coincides with a

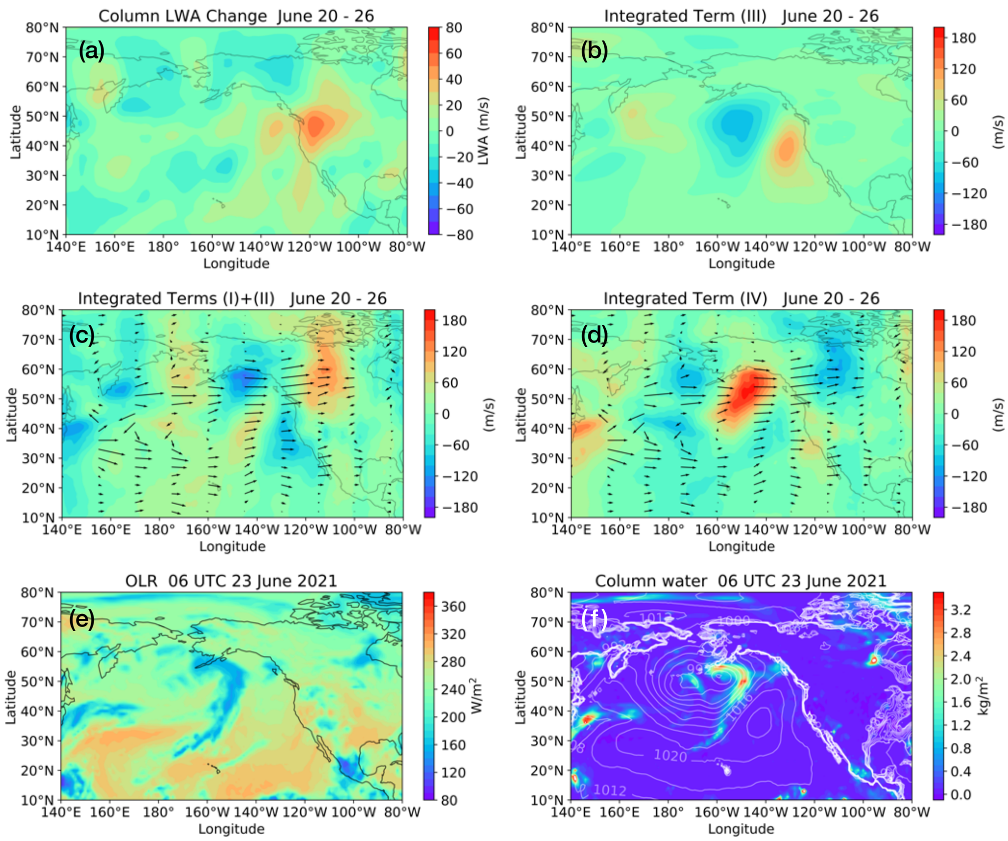

Figure 3. (a) Map of the LHS of Eq. (3) integrated from 20 to 26 June 2021 00 UTC. (b) Same as (a) but for Term (III). (c) Same as (b) but for Terms (I)+(II). (d) Same as (c) but for Term (IV). Arrows in (c) and (d) indicate the change in the 6-day average $(\langle F_\lambda \rangle, \langle F_{\phi'} \rangle)$ from the previous 6 days (14-20 June). The longest arrow is 40 $\mathrm{m^2 s^{-2}}$. For (a)-(d), a 10 degree running mean is applied in longitude to suppress noise. Note the different color scale for (a). (e) Outgoing longwave radiation at the top of the atmosphere at 06 UTC 23 June 2021. (f) Same as (e) but for column water (excluding vapor) and sea level pressure (in hPa).

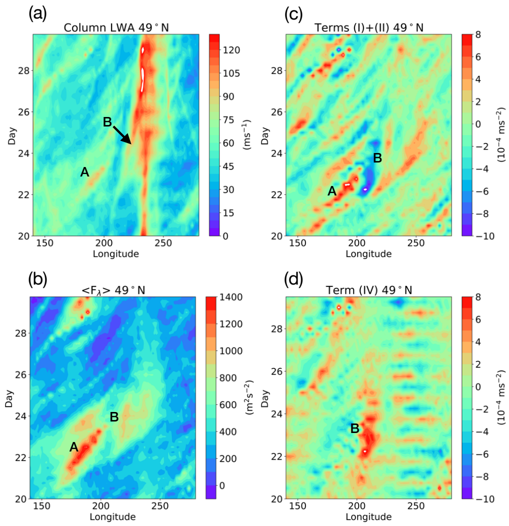

Figure 4. (a) Hovmöller diagram of column LWA at 49°N for 20-30 June 2021 00 UTC. (b) Same as (a) but for the column mean zonal wave activity flux $\langle F_\lambda \rangle$. (c) Same as (b) but for Terms (I)+(II) in Eq. (3). (d) Same as (c) but for Term (IV). A 10 degree running mean is applied in longitude for (c) and (d). The regularly spaced zonal striping in 225-270°E in (d) reflects the diurnal cycle in land-surface heating. See text for details.

strong flux divergence and a weak but persistent convergence immediately downstream (Fig. 4c). LWA that exits the region of divergence accumulates in the region of convergence, evidenced in Fig. 4a as a track of LWA emerges east of 200°E and eventually merges with the existing maximum at the Pacific Northwest. LWA achieves a peak intensity after the merger, 27-28 June.

To quantify the effect of the upstream diabatic source of wave activity on the downstream blocking, we integrate Eq. (3) at $\phi = 49°$N with a modified forcing. To this end, we first diagnose the zonal transport velocity $C(\lambda, t)$ and the diabatic forcing coefficient $\gamma(\lambda, t)$ for 20-26 June from the observed $\langle F_\lambda \rangle$, $\langle A \rangle$, $\langle \dot{A} \rangle$, using the following relations:

$$\langle F_\lambda \rangle = C \langle A \rangle \cos\phi, \quad \langle \dot{A} \rangle = \gamma \langle A \rangle, \quad \phi = 49°\text{N}. \tag{5}$$

We then modify γ such that any positive value in 200-220°E is decreased by 30 percent during 22-24 June. The change, $\Delta\gamma(\lambda, t)$, represents an artificial reduction of diabatic forcing in the region of cyclogenesis. Assuming that C, Terms (II) and (III) will not change, we may estimate the downstream influence of the perturbed forcing by rewriting Eq. (3) for the LWA perturbation (see Supporting Information):

$$\frac{\partial}{\partial t}\Delta\langle A \rangle = -\frac{1}{a\cos\phi}\frac{\partial\left(C\Delta\langle A \rangle\right)}{\partial \lambda} + \left(\gamma + \Delta\gamma\right)\Delta\langle A \rangle + \langle A \rangle \Delta\gamma, \quad \phi = 49°\text{N}. \tag{6}$$

We integrate Eq. (6) between 20-26 June from a zero initial condition. (C, γ and $\Delta\gamma$ are interpolated in time and we also add a small numerical diffusion.) The blue curve in Fig. 5 shows the observed change in column LWA between 20 and 26 June. The solid red curve is the predicted change for the same period with the modified forcing. The peak value is reduced by 41 percent and its location is displaced 10 degrees eastward (from 54.1 ms^{-1} at 242°E to 31.8 ms^{-1} at 252°E). When positive γ in 200-220°E is completely suppressed during 22-24 June, the change in LWA over the Pacific Northwest turns vastly negative (red dashed curve): instead of forming a block, the jet stream would become much less wavy.

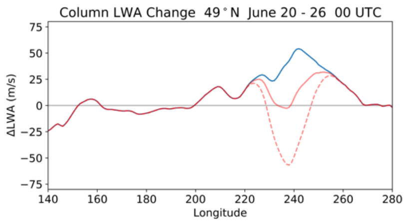

Figure 5. Blue: observed change in column LWA between 20 and 26 June 2021 00 UTC at 49°N. Solid-red: reconstructed change in column LWA with 70 percent of positive diabatic forcing in 200-220°E during 22-24 June. Dashed-red: Same as solid-red but with positive diabatic forcing completely suppressed in 200-220°E during 22-24 June.

5 Conclusions

We have identified the chain of events that led to the Pacific Northwest heat wave in late June - early July 2021: (i) cyclogenesis and associated wave breaking over the Gulf of Alaska (23-24 June), (ii) formation of a blocking anticyclone over the Pacific Northwest (24-27 June), and (iii) subsequent heating of surface (27-30 June). Our study suggests strong causal links between them: latent heating within the cyclone created an anomalous wave activity flux, which seeded the blocking anticyclone in the immediate downstream; and the stable stratification within the block suppressed convection and raised surface temperature. Other factors such as soil moisture deficit (Whan et al., 2015) and the foehn effect (Elvidge & Renfrew, 2016) may be important but are outside the scope of this work.

The absorption of incident wave activity flux from upstream has long been recognized as formation and maintenance mechanisms of blocks (Shutts, 1983; Mullen, 1987; H. Nakamura & Wallace, 1993; Luo, 2005; Yamazaki & Itoh, 2013; N. Nakamura & Huang, 2018), and the role of upstream cyclogenesis has also been reported for winter blocks (Colucci, 1985). These mechanisms are still at play in the 2021 event, but this event was unique in that the impact of latent heating over the upstream ocean manifested both dynamically and thermodynamically over a dry land in the downstream, where the small heat capacity of both ground and the block-capped boundary layer contributed to an unusual summertime heat event. Our result complements previous studies that suggest the influence of upstream latent heating on blocking based on trajectory analyses (Pfahl et al., 2015; Steinfeld & Pfahl, 2019). The LWA-based approach is particularly suited for the attribution of dynamical sources that contribute to the formation of a block.

The present analysis alone is insufficient to quantify the influence of climate change on the extreme events like this. However, to the extent that latent heating contributes to the strength of summer blocks and associated extreme heat, the severity of similar events will likely increase as the atmosphere warms and is loaded with more water vapor. Since the eastern North Pacific/Gulf of Alaska is a favorable location for block formation (Woollings et al., 2018), the risk for extreme heat in the Pacific Northwest will likely follow suit.

6 Open Research

ERA5 reanalysis data may be downloaded from `https://cds.climate.copernicus.eu/cdsapp#!/dataset/reanalysis-era5-pressure-levels?tab=overview`. The python code to compute LWA is found here: `https://github.com/csyhuang/hn2016_falwa`.

Acknowledgments

The bulk of this work has been conducted as EN's honors thesis at the Department of the Geophysical Sciences, University of Chicago, and supported by NSF Grant AGS1909522.

References

AON. (2021). *Global catastrophe recap september 2021.* Retrieved from `http://thoughtleadership.aon.com/Documents/20210012-analytics-if-september-global-recap.pdf`

Bueler, D., & Pfahl, S. (2017). Potential vorticity diagnostics to quantify effects of latent heating in extratropical cyclones. part i: Methodology. *Journal of the Atmospheric Sciences*, *74*, 3567-3590. doi: 10.1175/jas-d-17-0041.1

Colucci, S. J. (1985). Explosive cyclogenesis and large-scale circulation changes - implications for atmospheric blocking. *Journal of the Atmospheric Sciences*, *42*, 2701–2717. doi: 10.1175/1520-0469(1985)042⟨2701:ecalsc⟩2.0.co;2

Elvidge, A. D., & Renfrew, I. A. (2016). The causes of foehn warming in the lee of mountains. *Bulletin of the American Meteorological Society*, *97*, 455-466. doi: 10.1175/bams-d-14-00194.1

Fang, B., & Lu, M. (2020). Heatwave and blocking in the northeastern asia: Occurrence, variability, and association. *Journal of Geophysical Research-Atmospheres*, *125*(6), e2019JD031627. doi: 10.1029/2019jd031627

Hersbach, H., Bell, B., Berrisford, P., Hirahara, S., Horanyi, A., Munoz-Sabater, J., ... Thepaut, J. N. (2020). The era5 global reanalysis. *Quarterly Journal of the Royal Meteorological Society*, *146*(730), 1999–2049. doi: 10.1002/qj.3803

Huang, C. S. Y., & Nakamura, N. (2016). Local finite-amplitude wave activity as a diagnostic of anomalous weather events. *Journal of the Atmospheric Sciences*, *73*(1), 211–229. doi: 10.1175/JAS-D-15-0194.1

Huang, C. S. Y., & Nakamura, N. (2017). Local wave activity budgets of the wintertime northern hemisphere: Implication for the pacific and atlantic storm tracks. *Geophysical Research Letters*, *44*, 5673–5682. doi: 10.1002/2017GL073760

Luo, D.-H. (2005). Barotropic envelope rossby soliton model for block-eddy interaction. part i: Effect of topography. *Journal of the Atmospheric Sciences*, *62*, 5–21. doi: 10.1175/1186.1

Madonna, E., Wernli, H., Joos, H., & Martius, O. (2014). Warm conveyor belts in the era-interim dataset (1979-2010). part i: Climatology and potential vorticity evolution. *Journal of Climate*, *27*, 3-26. doi: 10.1175/jcli-d-12-00720.1

Methven, J. (2015). Potential vorticity in warm conveyor belt outflow. *Quarterly Journal of the Royal Meteorological Society*, *141*, 1065-1071. doi: 10.1002/qj.2393

Mullen, S. L. (1987). Transient eddy forcing of blocking flows. *Journal of the Atmospheric Sciences*, *44*, 3–22. doi: 10.1175/1520-0469(1987)044⟨0003:tefobf⟩2.0.co;2

Nakamura, H. (1994). Rotational evolution of potential vorticity associated with a strong blocking flow configuration over europe. *Geophysical Research Letters*, *21*, 2003–2006. doi: 10.1029/94GL01614

Nakamura, H., & Wallace, J. M. (1993). Synoptic behavior of baroclinic eddies during the blocking onset. *Monthly weather Review*, *121*, 1892–1903. doi: 10.1175/1520-0493(1993)121⟨1892:sbobed⟩2.0.co;2

Nakamura, N., & Huang, C. S. Y. (2018). Atmospheric blocking as a traffic jam in the jet stream. *Science*, *361*(6397), 42–47. doi: 10.1126/science.aat0721

Nakamura, N., & Solomon, A. (2010). Finite-amplitude wave activity and mean flow adjustments in the atmospheric general circulation. part i: Quasigeostrophic theory and analysis. *Journal of the Atmospheric Sciences*, *67*, 3967-3983. doi: 10.1175/2010jas3503.1

Nakamura, N., & Zhu, D. (2010). Finite-amplitude wave activity and diffusive flux of potential vorticity in eddy-mean flow interaction. *Journal of the Atmospheric Sciences*, *67*, 2701-2716. doi: 10.1175/2010jas3432.1

Pfahl, S., Schwierz, C., Croci-Maspoli, M., Grams, C. M., & Wernli, H. (2015). Importance of latent heat release in ascending air streams for atmospheric blocking. *Nature Geoscience*, *8*, 610–614. doi: 10.1038/ngeo2487

Philip, S. Y., Kew, S. F., van Oldenborgh, G. J., Anslow, F. S., Seneviratne, S. I., Vautard, R., ... Otto, F. E. L. (2021). Rapid attribution analysis of the extraordinary heatwave on the pacific coast of the us and canada june 2021. *Earth System Dynamics Discussions*, *2021*, 1–34. Retrieved from `https://esd.copernicus.org/preprints/esd-2021-90/` doi: 10.5194/esd-2021-90

Shutts, G. J. (1983). The propagation of eddies in difluent jetstreams: Eddy vorticity forcing of blocking flow fields. *Quarterly Journal of the Royal Meteorological Society*, *109*, 737-761. doi: 10.1002/qj.49710946204

Steinfeld, D., & Pfahl, S. (2019). The role of latent heating in atmospheric blocking dynamics: a global climatology. *Climate Dynamics*, *53*, 6159–6180. doi: 10.1007/s00382-019-04919-6

Valva, C., & Nakamura, N. (2021). What controls the probability distribution of local wave activity in the midlatitudes? *Journal of Geophysical Research - Atmospheres*, *126*, WOS:000683523400017. doi: 10.1029/2020jd034501

Whan, K., Zscheischler, J., Orth, R., Shongwe, M., Rahimi, M., Asare, E. O., & Seneviratne, S. I. (2015). Impact of soil moisture on extreme maximum temperatures in europe. *Weather and Climate Extremes*, *9*, 57-67. doi: 10.1016/j.wace.2015.05.001

Woollings, T., Barriopedro, D., Methven, J., Son, S. W., Martius, O., Harvey, B., et al. (2018). Blocking and its response to climate change. *Current Climate Change Reports*, *4*(3), 287–300. doi: 10.1007/s40641-018-0108-z

Yamazaki, A., & Itoh, H. (2013). Vortex-vortex interactions for the maintenance of blocking. part i: The selective absorption mechanism and a case study. *Journal of the Atmospheric Sciences*, *70*, 725-742. doi: 10.1175/jas-d-11-0295.1

Supporting Information for "The 2021 Pacific Northwest heat wave and associated blocking: meteorology and the role of an upstream cyclone as a diabatic source of wave activity"

Emily Neal [1], Clare S. Y. Huang [1] and Noboru Nakamura [1]

[1]Department of the Geophysical Sciences, University of Chicago

Contents of this file

1. Computing local wave activity (LWA) from ERA5 reanalysis data
2. Evaluating the column LWA with ERA5 reanalysis data
3. Formulation of one-dimensional model for reconstructing LWA with modified forcing

Introduction This document describes some technical aspects of local wave activity (LWA) diagnostic. The formalism itself is laid out in the Supporting Information of Huang and Nakamura (2017, hereafter S17), and that document is still a good starting point for the reader unfamiliar with the diagnostic procedure. The present document recaps some of the basics but mostly highlights applications specific to ERA5 (Hersbach et al., 2020). We will also describe the formulation of a one-dimensional model to reconstruct LWA with modified forcing (Fig. 5 of main text).

Computing local wave activity (LWA) from ERA5 reanalysis data

The LWA diagnostic used in the present (and most previous) work is built on the quasi-geostrophic theory, and as such, the key quantity is quasigeostrophic potential vorticity (QGPV). It is well known that some of the assumptions for the QG theory do not hold accurately on a sphere even in the extratropics (e.g. deviation of the Coriolis parameter from a constant must be on the order of the Rossby number), and we do not attempt to fill those gaps. We will keep the Coriolis parameter f a full function of latitude and use full vorticity instead of geostrophic vorticity to define an 'approximate' QGPV. In practical terms, we use the horizontal velocity and (potential) temperature from reanalysis data (u, v, θ) to compute QGPV as

$$q(\lambda, \phi, z, t) = f + \frac{1}{a\cos\phi}\left(\frac{\partial v}{\partial \lambda} - \frac{\partial(u\cos\phi)}{\partial\phi}\right) + fe^{z/H}\frac{\partial}{\partial z}\left(\frac{e^{-z/H}(\theta - \tilde{\theta})}{\partial\tilde{\theta}/dz}\right). \tag{1}$$

In the above, (λ, ϕ, z, t) denote longitude, latitude, pressure pseudoheight and time, respectively, $z = -H\ln(p/1000\text{hPa})$ (p is pressure and $H = 7$ km is assumed), $f = 2\Omega\sin\phi$, $a = 6378$ km and $\Omega = 7.29\times10^{-5}$ rad s^{-1} are the radius and rotation rate of the planet. $\tilde{\theta}(z, t)$ is hemispheric mean potential temperature. It is computed from instantaneous values, but its time dependence is generally very weak, consistent with the QG theory. To evaluate Eq. (1) we first vertically interpolate (u, v, θ) from the 37 pressure levels of ERA5 onto uniformly spaced z-surfaces — in our case with a 500 m interval — up to $z = 48$ km. (We use this coordinate to maintain sufficient details in the stratosphere, but for the column budget this is not necessary, since the stratosphere does not contribute much to the density weighted vertical average — one may well formulate Eq. (1) with the pressure coordinate in the vertical.) We then use finite difference to evaluate Eq. (1) [S17 Eq. (5)].

LWA is defined as

$$A(\lambda, \phi, z, t) = -\frac{a}{\cos\phi}\int_0^{\Delta\phi} q_e(\lambda, \phi + \phi', z, t)\cos(\phi + \phi')d\phi', \tag{2}$$

$$q_e(\lambda, \phi + \phi', z, t) = q(\lambda, \phi + \phi', z, t) - q_{\mathrm{REF}}(\phi, z, t). \tag{3}$$

To evaluate Eq. (2) one must first evaluate Eq. (3), and to evaluate Eq. (3) one must evaluate q_{REF}. We compute q_{REF} by zonalizing the instantaneous QGPV field through an area-preserving map. The easiest way to do this is to first evaluate Eq. (1) for both hemispheres and create a global map of QGPV for each z-surface. With $1° \times 1°$ horizontal resolution, there are 360×180 grid points, indexed by (i, j). At each z and t, all grid points (i, j) are sorted according to equally spaced 181 values of q between the minimum and maximum values on that level $[Q_n = (n-1)\Delta Q,\ 1 \le n \le 181,\ \Delta Q = (\max(q_{ij}) - \min(q_{ij}))/180]$. Because of f, typically the minimum value of $q(\lambda, \phi)$ is found near the South Pole, and the maximum value is found near the North Pole. We then compute the area of the region in which $q_{ij} \ge Q_n$ $[\equiv A_n(Q_n)]$ by conditional box counting, weighting each grid with a fractional area $a^2 \cos\phi_j (\Delta\lambda)^2$ $(\Delta\lambda = \pi/180)$. The area $A_n(Q_n)$ is then mapped to equivalent latitude with the formula

$$\phi_n(Q_n) = \sin^{-1}\left(1 - \frac{A_n}{2\pi a^2}\right), \tag{4}$$

which effectively associates the minimum QGPV with the South Pole and the maximum QGPV with the North Pole. Finally by inverting this one-to-one relationship between latitude and QGPV, one obtains $q_{\mathrm{REF}}(\phi)$ at given z and t.

Note that q_e in Eq. (3) must be reevaluated for different ϕ, because q_e is q relative to a value of q_{REF} *at a certain latitude* ϕ. Since q_{REF} increases with latitude, $q_e < 0$ where the QGPV contour $q(\lambda, \phi + \phi') = q_{\mathrm{REF}}(\phi)$ is displaced northward from ϕ (i.e. $\phi' > 0$), and $q_e > 0$ where it is displaced southward ($\phi' < 0$). Either way Eq. (2) is positive. Care must be taken where $\Delta\phi$ is multivalued due to an overturned or cutoff QGPV contour. To take care of this situation automatically, the line integral in Eq. (2) is evaluated at each longitude by scanning the entire latitudes from the South Pole to the North Pole, collecting all contribution from ($q_e < 0,\ \phi' > 0$) and ($q_e > 0,\ \phi' < 0$) (see Fig. 1 of Huang & Nakamura, 2016).

Evaluating the column LWA budget with ERA5 reanalysis data

The column budget of LWA reads

$$\frac{\partial}{\partial t}\langle A\rangle\cos\phi = \underbrace{-\frac{1}{a\cos\phi}\frac{\partial\langle F_\lambda\rangle}{\partial\lambda}}_{\text{(I)}}\underbrace{-\frac{1}{a\cos\phi}\frac{\partial}{\partial\phi'}\langle F_{\phi'}\cos(\phi+\phi')\rangle}_{\text{(II)}}\underbrace{+\frac{f\cos\phi}{H}\left(\frac{v_e\theta_e}{\partial\tilde{\theta}/\partial z}\right)_{z=0}}_{\text{(III)}}\underbrace{+\langle\dot{A}\rangle\cos\phi}_{\text{(IV)}}, \tag{5}$$

$$\langle F_\lambda\rangle = \langle u_{\mathrm{REF}}A\cos\phi\rangle - a\left\langle\int_0^{\Delta\phi} u_e q_e\cos(\phi+\phi')d\phi'\right\rangle + \frac{\cos\phi}{2}\left\langle v_e^2 - u_e^2 - \frac{R}{H}\frac{e^{-\kappa z/H}\theta_e^2}{\partial\tilde{\theta}/\partial z}\right\rangle, \tag{6}$$

$$\langle F_{\phi'}\rangle = -\langle u_e v_e\cos(\phi+\phi')\rangle. \tag{7}$$

Note that the RHS terms in Eq. (5) are evaluated at $\phi' = 0$. In the above the angle bracket denotes density-weighted vertical average, R is gas constant and $\kappa = R/c_p$ (c_p is specific heat at constant pressure). The contribution of the last term of Eq. (6) to Term (I), plus Terms (II) and (III) constitutes the vertical average of Eliassen-Palm flux divergence, or equivalently, $\cos\phi\langle v_e q_e\rangle$ via Taylor's identity. Note also

$$u_e(\lambda, \phi+\phi', z, t) = u(\lambda, \phi+\phi', z, t) - u_{\mathrm{REF}}(\phi, z, t), \tag{8}$$

$$v_e(\lambda, \phi + \phi', z, t) = v(\lambda, \phi + \phi', z, t), \tag{9}$$

$$\theta_e(\lambda, \phi + \phi', z, t) = \theta(\lambda, \phi + \phi', z, t) - \theta_{\mathrm{REF}}(\phi, z, t), \tag{10}$$

where $(u_{\mathrm{REF}}, \theta_{\mathrm{REF}})$ are the reference-state zonal wind and potential temperature, and they must be inverted (hemispherically) from $q_{\mathrm{REF}}(\phi, z, t)$. $(u_{\mathrm{REF}}, \theta_{\mathrm{REF}})$ is related to q_{REF} through

$$q_{\mathrm{REF}}(\mu, z, t) = 2\Omega\mu - \frac{1}{a}\frac{\partial}{\partial\mu}\left(u_{\mathrm{REF}}\cos\phi\right) + 2\Omega\mu e^{z/H}\frac{\partial}{\partial z}\left(\frac{e^{-z/H}(\theta_{\mathrm{REF}} - \tilde{\theta})}{\partial\tilde{\theta}/\partial z}\right), \tag{11}$$

where $\mu \equiv \sin\phi$. Using thermal wind balance

$$2\Omega\mu\frac{\partial}{\partial z}\left(u_{\mathrm{REF}}\cos\phi\right) = -\frac{R(1-\mu^2)e^{-\kappa z/H}}{Ha}\frac{\partial\theta_{\mathrm{REF}}}{\partial\mu}, \tag{12}$$

Eq. (11) may be transformed into an elliptic equation for $u_{\mathrm{REF}}\cos\phi$

$$\frac{\partial}{\partial\mu}\left[\frac{1}{2\Omega\mu}\frac{\partial(u_{\mathrm{REF}}\cos\phi)}{\partial\mu}\right] + \frac{2\Omega Ha^2\mu}{R(1-\mu^2)}e^{z/H}\frac{\partial}{\partial z}\left[e^{(\kappa-1)z/H}\frac{\partial(u_{\mathrm{REF}}\cos\phi)/\partial z}{\partial\tilde{\theta}/\partial z}\right] = -a\frac{\partial}{\partial\mu}\left(\frac{q_{\mathrm{REF}}}{2\Omega\mu}\right). \tag{13}$$

We solve Eq. (13) hemispherically on a uniform grid in (μ, z) for $z \in [0, 48]$ km, $\mu \in [0.0872, 1]$. We have also solved Eq. (13) with uniform ϕ and obtained a virtually identical result. Note we set the southernmost boundary of the domain at $\phi = 5°$N to avoid the difficulty with a vanishing μ at the equator. Avoiding the equator proves particularly important for high-resolution data to ensure the convergence of inversion algorithm. The boundary conditions are:

$$u_{\mathrm{REF}}\cos\phi = 0 \quad \text{at} \quad \mu = 1 \quad \text{and} \quad z = 0 \tag{14}$$

$$2\Omega\mu\frac{\partial}{\partial z}\left(u_{\mathrm{REF}}\cos\phi\right) = -\frac{R(1-\mu^2)e^{-\kappa z/H}}{Ha}\frac{\partial[\theta]}{\partial\mu} \quad \text{at} \quad z = 48 \text{ km} \tag{15}$$

$$u_{\mathrm{REF}}\cos\phi = (K - 2\pi\Omega a^2\cos^2\phi)/2\pi a \quad \text{at} \quad \mu = 0.0872\ (\phi = 5°\text{N}). \tag{16}$$

In the above, $[\theta]$ denotes the zonal-mean potential temperature at $z = 48$ km, and $K(z,t)$ is Kelvin's circulation at 5°N equivalent latitude. K is evaluated as the surface integral of absolute vorticity over the domain where QGPV is greater than q_{REF} at 5°N. Since Kelvin's circulation around the QGPV contour is nearly conservative, this boundary condition does not introduce spurious eddy forcing. We have tested different boundary conditions at 5°N and found that they do not affect u_{REF} in the extratropics very much. The no-slip boundary condition at the lower boundary is chosen because u_{REF} represents an eddy-free reference state: a nonzero surface wind requires eddy momentum flux in the presence of surface friction and incompatible with the notion of eddy-free state (Nakamura & Solomon, 2010).

Once we obtain u_{REF}, we reconstruct θ_{REF} using the thermal wind balance [Eq. (12)]. At each altitude a constant value is added to θ_{REF} so that its hemispheric mean matches $\tilde{\theta}(z,t)$. After obtaining $(u_{\mathrm{REF}}, \theta_{\mathrm{REF}})$ we can compute (u_e, θ_e) from Eqs. (8) and (10) and finally evaluate the terms in Eq. (5). We approximate the density weighted vertical average $\langle \cdots \rangle$ as

$$\langle (\cdots) \rangle = \frac{\int (\cdots) e^{-z/H} dz}{H} \approx \frac{\sum_{k=2}^{96} (\cdots)_k e^{-z_k/H} \Delta z}{\sum_{k=2}^{96} e^{-z_k/H} \Delta z} = \frac{\sum_{k=2}^{96} (\cdots)_k e^{-z_k/H} \Delta z}{6.745\mathrm{km}}, \quad \Delta z = 500 \text{ m}. \tag{17}$$

Note that $H = 7$ km in the denominator is replaced by 6.745 km due to discretization. With this approximation, Term (III) in Eq. (5) consists of contributions from k = 1 and 2 ($z = 0$ and 500 m) due to the form of the vertical discretization of QGPV [S17 Eq. (5)]:

$$\frac{f \cos\phi}{H} \left(\frac{v_e \theta_e}{\partial \tilde{\theta} / \partial z} \right)_{z=0} \approx \frac{2\Omega \sin\phi_j \cos\phi_j}{6.745\mathrm{km}} \left(\frac{e^{-z_2/H} v_{eij2} \theta_{eij2}}{\tilde{\theta}_3 - \tilde{\theta}_1} + \frac{v_{eij1} \theta_{eij1}}{2(\tilde{\theta}_2 - \tilde{\theta}_1)} \right) \Delta z. \tag{18}$$

In S17 we conducted several different methods to evaluate the lowest level temperatures in reanalysis and found the result to be insensitive to the chosen methods except for regions with high topography.

Formulation of one-dimensional model for reconstructing LWA with modified forcing

To evaluate the impact of upstream forcing on the downstream block formation, we first evaluate the terms in Eq. (5) using data at a given latitude ϕ for a given period. We can then estimate the zonal transport velocity for column LWA $C(\lambda, t)$ and forcing coefficient $\gamma(\lambda, t)$ from the observed $\langle F_\lambda \rangle$, $\langle A \rangle$, $\langle \dot{A} \rangle$, using the following relationships:

$$\langle F_\lambda \rangle = C \langle A \rangle \cos\phi, \quad \langle \dot{A} \rangle \cos\phi = \gamma \langle A \rangle \cos\phi. \tag{19}$$

With Eq. (19), Eq. (5) may be rewritten as

$$\frac{\partial}{\partial t} \langle A \rangle \cos\phi = -\frac{1}{a\cos\phi} \frac{\partial \left(C \langle A \rangle \cos\phi \right)}{\partial \lambda} + \text{Term (II)} + \text{Term (III)} + \gamma \langle A \rangle \cos\phi. \tag{20}$$

Now we perturb γ to $\gamma + \Delta\gamma$, and as a result $\langle A \rangle$ is also perturbed to $\langle A \rangle + \Delta \langle A \rangle$, but for simplicity we assume that C, Term (II) and Term (III) do not change. (We found little correlation between C and $\langle A \rangle$ during 20-26 June at 49°N.) The above equation is then modified to

$$\begin{aligned} \frac{\partial}{\partial t} \left(\langle A \rangle + \Delta \langle A \rangle \right) \cos\phi = & -\frac{1}{a\cos\phi} \frac{\partial \left[C \left(\langle A \rangle + \Delta \langle A \rangle \right) \cos\phi \right]}{\partial \lambda} \\ & + \text{Term (II)} + \text{Term (III)} + (\gamma + \Delta\gamma) \left(\langle A \rangle + \Delta \langle A \rangle \right) \cos\phi. \end{aligned} \tag{21}$$

Subtracting Eq. (20) from Eq. (21) and dividing by $\cos\phi$,

$$\frac{\partial}{\partial t} \Delta \langle A \rangle = -\frac{1}{a\cos\phi} \frac{\partial \left(C \Delta \langle A \rangle \right)}{\partial \lambda} + (\gamma + \Delta\gamma) \Delta \langle A \rangle + \langle A \rangle \Delta\gamma. \tag{22}$$

We solve Eq. (22) for $\Delta\langle A\rangle$ with the knowledge of C, γ, $\Delta\gamma$ and $\langle A\rangle$. In practice, we interpolate these four parameters onto a smaller time interval of 10 minutes, and add a small second-order diffusion with a diffusion coefficient of 2×10^5 $\mathrm{m^2s^{-1}}$ to keep the solution smooth.

References

Hersbach, H., Bell, B., Berrisford, P., Hirahara, S., Horanyi, A., Munoz-Sabater, J., ... Thepaut, J. N. (2020). The era5 global reanalysis. *Quarterly Journal of the Royal Meteorological Society*, *146*(730), 1999–2049. doi: 10.1002/qj.3803

Huang, C. S. Y., & Nakamura, N. (2016). Local finite-amplitude wave activity as a diagnostic of anomalous weather events. *Journal of the Atmospheric Sciences*, *73*(1), 211–229. doi: 10.1175/JAS-D-15-0194.1

Huang, C. S. Y., & Nakamura, N. (2017). Local wave activity budgets of the wintertime northern hemisphere: Implication for the pacific and atlantic storm tracks. *Geophysical Research Letters*, *44*, 5673–5682. doi: 10.1002/2017GL073760

Nakamura, N., & Solomon, A. (2010). Finite-amplitude wave activity and mean flow adjustments in the atmospheric general circulation. part i: Quasigeostrophic theory and analysis. *Journal of the Atmospheric Sciences*, *67*, 3967-3983. doi: 10.1175/2010jas3503.1